UNIVERSITY OF TROMSØ UIT

FACULTY OF SCIENCE AND TECHNOLOGY
DEPARTMENT OF MATHEMATICS AND STATISTICS

# Statistical Analysis of Lattice Data with Wavelet Variance Methods and Spatiotemporal Modeling of Infectious Disease Spread

Marc Geilhufe

A dissertation for the degree of Philosophiae Doctor

May 2013

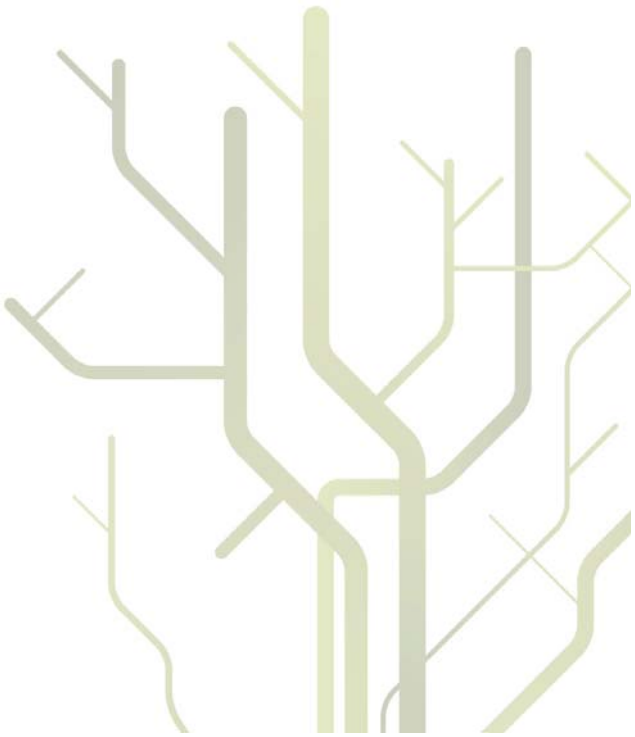

## ABSTRACT

The field of spatial statistics has been growing steadily in the last decades. Increasing computational resources make it feasible to do statistical analysis of huge spatial and spatiotemporal data sets across many disciplines such as climatology, epidemiology or geology. Real world processes are put into a model framework to describe observations in space and time. One part in spatial statistics, and the focus of this thesis, is the analysis of lattice data. Both regular and irregular lattice data are of interest. The first is addressed in Papers I and II by wavelet-based methods for random fields and the latter in Paper III by spatiotemporal modeling of infectious disease spread in North Norway.

Paper I describes an extension of the pyramid algorithm for efficient Maximal Overlap Discrete Wavelet Transform (MODWT) coefficient calculation. As opposed to common usage of two-dimensional wavelet decomposition, it here also allows for different scales in the vertical and horizontal direction. Wavelet variances, i.e., the variances of the wavelet coefficient processes, are investigated for scale-dependent analysis of spatial patterns. A practical geoscience application with Synthetic Aperture Radar (SAR) images of sea ice illustrates its potential. Physical changes of the sea ice over the course of one year are connected with changes in statistical properties of its SAR images.

Paper II uses much of the same underlying theory as Paper I. Here, wavelet variances are used to develop a novel test for isotropy of random fields. Isotropy is frequently assumed in spatial modeling. It requires the covariance or variogram function of a stationary or intrinsically stationary spatial process to depend only on the distance between two locations, independent of direction. In a simulation study, the presented test for isotropy is applied to realizations of various isotropic and anisotropic Gaussian random fields. Its performance is superior compared to existing methods, both on the general applicability and the consistent rejection rate close to the nominal level for isotropic fields, while the power for anisotropic fields is comparable to or better than other methods. Furthermore, an example connected to the manufacturing of paper also demonstrates practical applicability of the wavelet-based isotropy test.

In Paper III microbiology test results of influenza A disease counts in the sparsely populated municipalities of North Norway are modeled to study the pattern of disease spread. The focus is to link the disease incidence to movement networks, with human travel patterns described by actual traffic data or a power law approach. Models with fixed, seasonal and random effects are used and extended with covariates accounting for different population sizes in the municipalities, reporting bias and immigration from outside the considered region. An additional analysis is performed by grouping the data into adults and non-adults. All models are compared by one-step-ahead predictions using proper scoring rules.

# ACKNOWLEDGMENTS

The achievements in this thesis would not have been possible without the help and support of several people. I had a great time in Tromsø and will always remember this magnificent Arctic place with joy. First of all I would like to thank my main supervisor at University of Tromsø (UiT), Professor Fred Godtliebsen. He was always available for helpful discussions and positive input. Fred strongly supported my development during the Ph.D. period, enabling my attendance to several conferences as well as two research visits in the USA and one in Switzerland. Next, my sincere gratitude goes to my co-supervisor Professor Donald Percival at the University of Washington (UW) in Seattle, USA. Don gave me the possibility to visit UW in July–December 2010 and November/December 2011. He introduced me to the world of wavelets and I am grateful for all the help, ideas and advice I have received from him. The collaboration with him was excellent right from the beginning and resulted in two papers that are part of this Ph.D. thesis. I am also thankful to my co-supervisors Stein Olav Skrøvseth at the Norwegian Centre for Integrated Care and Telemedicine (NST) and Professor Håvard Rue at the Norwegian University of Science and Technology (NTNU) in Trondheim. Stein Olav was always around for discussions and finding solutions to all kinds of obstacles that occurred in the different projects. Håvard was available for discussions during regular visits in Tromsø and gave me remote access to an extremely powerful server at NTNU, which was truly helpful for the extensive calculations in Papers II and III.

In July 2012 I visited the Division of Biostatistics at University of Zurich, Switzerland. This stay was initiated by Andrea Riebler after discussing my research at a conference in Trondheim. She was kind enough to present my problems to Professor Leonhard Held, who offered me to come to Zurich. The excellent collaboration with Leo and his research group was the key to the developments in Paper III of this thesis. Here I would also like to thank Sebastian Meyer and Michaela Paul for all the advice in disease modeling with the `surveillance` package in `R`.

What would the Ph.D. period be without good colleagues that you share your life with every day? Fortunately I was lucky enough to have the best colleagues in the world that became also good friends. You made my workday life very comfortable. I am going to miss the Sporcle quizzes and the common lunches hoping for a good "dagens". With Kevin I spent the most time together as office mates, both in Tromsø and Seattle. This superb team work resulted in Paper II of this thesis. Kristian joined the office in 2012, which was a real enrichment for everybody. He has helped me a lot, from small programming issues to proofreading of the entire thesis, tusen takk! I would also like to thank Jörn, Kajsa, Maciel and many others at Tromsø Telemedicine Laboratory (TTL), NST and UiT for the nice time I had here.

Last but not least I would like to express my sincere gratitude to my family back home in Germany and to my friends from all over the world. Thank you for your support and enriching my life also outside the work on the Ph.D.

# LIST OF PUBLICATIONS

**Paper I** Two-dimensional wavelet variance estimation with application to sea ice SAR images, **Geilhufe, M., Percival, D. B. and Stern, H. L.**, *Computers & Geosciences*, 2013, Vol. 54, pp. 351-360

**Paper II** A multiscale wavelet-based test for isotropy of random fields on a regular lattice, **Thon K., Geilhufe, M. and Percival, D. B.**, submitted to *IEEE Transactions on Image Processing*

**Paper III** Power law approximations of movement network data for modeling infectious disease spread, **Geilhufe, M., Held, L., Skrøvseth, S. O., Simonsen, G. S. and Godtliebsen, F.**, revised and re-submitted to *Biometrical Journal*

# CONTENTS

Part I

# INTRODUCTION PART

# 1

# INTRODUCTION

Spatial statistics is a broad field, where spatial patterns are reduced to clear and useful summaries, and compared with expectations from theory about their potential origin and development (Ripley, 1981). Spatial models are applied in a variety of disciplines such as climatology and geology (Chilès and Delfiner, 2012), epidemiology (Lawson, 2006) or image processing (Gonzalez and Woods, 2008). Data are collected from different spatial locations $\boldsymbol{s}$ that follow a *spatial process* $\{X(\boldsymbol{s}) : \boldsymbol{s} \in D\}$, where $D$ is a subset of the $d$-dimensional Euclidean space, $D \subset \mathbb{R}^d$. It can be extended to a *spatiotemporal process* $\{X(\boldsymbol{s},t) : \boldsymbol{s} \in D(t),\ t \in T\}$ with time $t$ from domain $T \in \mathbb{R}$. Cressie (1993) categorizes spatial data into geostatistical data, point patterns and lattice data. In the first category the spatial index $\boldsymbol{s}$ varies continuously over a region $D$. For point patterns the focus is the location of spatial events, hence to determine whether the pattern shows spatial randomness, clustering or regularity. Lattice data are used, e.g., for image restoration, quantifying spatial correlations, or constructing and analyzing explicative models (Gaetan and Guyon, 2010). Here the data depend on properties of their locations, which Cressie (1993) groups into (i) regular or irregular, (ii) points or regions and (iii) indices for continuous or discrete random variables.

The focus of this thesis is statistical analysis of lattice data, where the locations represent:

1. Regular point indices for continuous random variables,

2. Irregular region indices for discrete random variables.

Papers I & II address the first point and present analyses of wavelet variances for random fields on a regular lattice. Related basic terminology and motivation is introduced in Section 1.1. In Paper III the second point is addressed by comparing models for person-to-person transmitted infectious disease spread in North Norway incorporating human travel patterns. Section 1.2 provides an introduction to the spatiotemporal data used in Paper III. All papers are summarized and discussed in Section 2. The main part of this thesis is Part II which contains the full manuscripts of Papers I, II and III.

## 1.1 WAVELET VARIANCE ANALYSIS

### 1.1.1 *General definitions*

First, necessary terms will be defined. Let $\{X(\boldsymbol{s}) = X_{u,v} : \boldsymbol{s} = (u,v) \in \mathbb{Z}^2\}$ denote a *random field* or *random process* on a regular two-dimensional lattice. An important class of random processes is *Gaussian fields*. Here, for any location $\boldsymbol{s}_1, ..., \boldsymbol{s}_k \in \mathbb{Z}^2$, $[X(\boldsymbol{s}_1), ..., X(\boldsymbol{s}_k)]^T$ is normally distributed with mean $\mu(s) = E\{X(s)\}$ and covariance $C(\boldsymbol{s}_i, \boldsymbol{s}_j) = \text{cov}\{X(\boldsymbol{s}_i), X(\boldsymbol{s}_j)\}$ for all $\boldsymbol{s}_i, \boldsymbol{s}_j \in \mathbb{Z}^2$.

A random field is *second-order stationary* (also known as *weakly* or *wide-sense stationary*), henceforth denoted as *stationary*, when it has constant mean $E(X_{u,v}) = \mu$ and the covariance between its elements depends only on the relative displacement of the locations, i.e., $C(\boldsymbol{s}, \boldsymbol{s} + \boldsymbol{\kappa}) = C(\boldsymbol{\kappa}) = \text{cov}\{X_{u,v}, X_{u+\kappa_1, v+\kappa_2}\}$ for all lags $\boldsymbol{\kappa} = (\kappa_1, \kappa_2) \in \mathbb{Z}^2$. If only the increment process $\{X_{u,v} - X_{u+\kappa_1, v+\kappa_2}\}$ is stationary, then $\{X_{u,v}\}$ is called *intrinsically stationary*. In this case the increments have finite variances, which are expressed by *semivariogram* $\gamma(\boldsymbol{\kappa}) = \gamma_{X,\kappa_1,\kappa_2} = \frac{1}{2}\text{var}\{X_{u,v} - X_{u+\kappa_1, v+\kappa_2}\}$, or *variogram* $2\gamma(\boldsymbol{\kappa})$ respectively. The variogram is a structure function that describes how the values at two points become different with increasing separation between the points (Chilès and Delfiner, 2012). For stationary processes, the following relation is valid: $\gamma(\boldsymbol{\kappa}) = \frac{1}{2}(C(0) - C(\boldsymbol{\kappa}))$.

If the semivariogram of a (intrinsically) stationary process $\{X_{u,v}\}$ is only a function of the distance between two locations, i.e., $\gamma(\boldsymbol{\kappa}) = \gamma(||\boldsymbol{\kappa}||)$, then $\{X_{u,v}\}$ is called *isotropic*, otherwise *anisotropic*. Stationary isotropic processes can also be expressed in terms of the covariance function not being dependent on direction, i.e., $C(\boldsymbol{\kappa}) = C(||\boldsymbol{\kappa}||)$. In Paper II a test for isotropy is presented based on wavelet variances over different scales. See the next section for an introduction to the necessary wavelet theory.

### 1.1.2 *Wavelets*

Throughout this thesis wavelet coefficients are obtained by the Maximal Overlap Discrete Wavelet Transform (MODWT), which is characterized by the fact that it does not involve sub-sampling of the output, as opposed to the commonly used Discrete Wavelet Transform (DWT). Thus the coefficient processes are of the same size as the input for all wavelet levels.

In one dimension, e.g., the time-series case, the MODWT is based on two unit-level filters known as the wavelet filter $\{h_{1,l}\}$ and scaling filter $\{g_{1,l}\}$, each of which is of even length $L$. The

most common and here used filters are of the Daubechies class (Daubechies, 1992), meaning they satisfy

$$\sum_{l=0}^{L-1} h_{1,l} = 0, \quad \sum_{l=0}^{L-1-2n} h_{1,l}h_{1,l+2n} = 0, \;\; n = 1,\ldots,\frac{L}{2}-1, \;\; \text{and} \;\; g_{1,l} = (-1)^{l+1}h_{1,L-1-l} \; .$$

The wavelet filters $\{h_{j,l}\}$ perform differencing operations, whereas averages are obtained with the scaling filters $\{g_{j,l}\}$. The simplest example is the Haar wavelet ($L = 2$), for which $h_{1,0} = 1/2 = -h_{1,1}$. Other Daubechies filters used in this thesis are the D(4) wavelet of length $L = 4$ and the least asymmetric filter of length $L = 8$, LA(8). See Fig. 1 for an example plot of these wavelet and scaling filters.

Let $H_1(\cdot)$ and $G_1(\cdot)$ denote the transfer functions of $\{h_{1,l}\}$ and $\{g_{1,l}\}$, i.e.,

$$H_1(f) = \sum_{l=0}^{L-1} h_{1,l}e^{-i2\pi fl} \quad \text{and} \quad G_1(f) = \sum_{l=0}^{L-1} g_{1,l}e^{-i2\pi fl}.$$

The unit-level filters can be used to create the $j$th level wavelet filter $\{h_{j,l}\}$ and scaling filter $\{g_{j,l}\}$ via the inverse Fourier transforms of

$$H_j(f) = H_1(2^{j-1}f)\prod_{l=0}^{j-2} G_1(2^l f) \;\; \text{and} \;\; G_j(f) = \prod_{l=0}^{j-1} G_1(2^l f).$$

These $j$th level filters have length $L_j = (2^j - 1)(L-1) + 1$ and are normalized such that

$$\sum_{l=0}^{L_j-1} h_{j,l}^2 = \sum_{l=0}^{L_j-1} g_{j,l}^2 = 1/2^j.$$

Level $j$ is a scale index, with the scale being given by $\tau_j = 2^{j-1}$ for $\{h_{j,l}\}$ and by $2\tau_j = 2^j$ for $\{g_{j,l}\}$ (for details see, e.g., Percival and Walden, 2000).

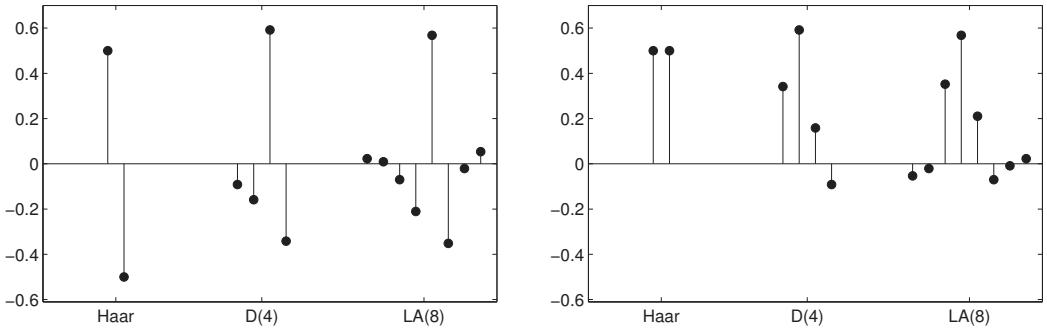


(a) Wavelet filters (b) Scaling filters

Figure 1: Illustration of three different sets of unit-level MODWT wavelet and scaling filters.

In two dimensions, for a random field $\{X_{u,v}\}$ usually a tensor product of the one-dimensional wavelet and scaling filters is used to define different two-dimensional wavelet coefficient processes (Mondal and Percival, 2012b), i.e., wavelet-wavelet (ww) $\{W_{j,j'}(u,v) : (u,v) \in \mathbb{Z}^2\}$, scaling-wavelet (sw) $\{U_{j,j'}(u,v) : (u,v) \in \mathbb{Z}^2\}$, wavelet-scaling (ws) $\{V_{j,j'}(u,v) : (u,v) \in \mathbb{Z}^2\}$ and scaling-scaling (ss) coefficient process $\{Z_{j,j'}(u,v) : (u,v) \in \mathbb{Z}^2\}$:

$$W_{j,j'}(u,v) = \sum_{l=0}^{L_j-1} \sum_{l'=0}^{L_{j'}-1} h_{j,l} h_{j',l'} X_{u-l,v-l'}, \tag{1}$$

$$U_{j,j'}(u,v) = \sum_{l=0}^{L_j-1} \sum_{l'=0}^{L_{j'}-1} g_{j,l} h_{j',l'} X_{u-l,v-l'}, \tag{2}$$

$$V_{j,j'}(u,v) = \sum_{l=0}^{L_j-1} \sum_{l'=0}^{L_{j'}-1} h_{j,l} g_{j',l'} X_{u-l,v-l'}, \tag{3}$$

$$Z_{j,j'}(u,v) = \sum_{l=0}^{L_j-1} \sum_{l'=0}^{L_{j'}-1} g_{j,l} g_{j',l'} X_{u-l,v-l'}. \tag{4}$$

For the wavelet-wavelet coefficients $W_{j,j'}(u,v)$, wavelet filters are applied both to rows at scale $\tau_j$ and columns at scale $\tau_{j'}$, capturing simultaneously both horizontal and vertical (thus diagonal) structure. $U_{j,j'}(u,v)$ coefficients are the result of averaging the rows at scale $2\tau_j$ and differencing the columns at scale $\tau_{j'}$, i.e., $U_{j,j'}(u,v)$ calculates a horizontal difference, which makes it capture vertical structure. The opposite is done with $V_{j,j'}(u,v)$, focusing on horizontal structure. $Z_{j,j'}(u,v)$ contains only averages, which makes it the least interesting part. However, it is needed to calculate higher level coefficients.

Using the Haar wavelet, it is illustrated in Fig. 2 how the different filter operations manipulate

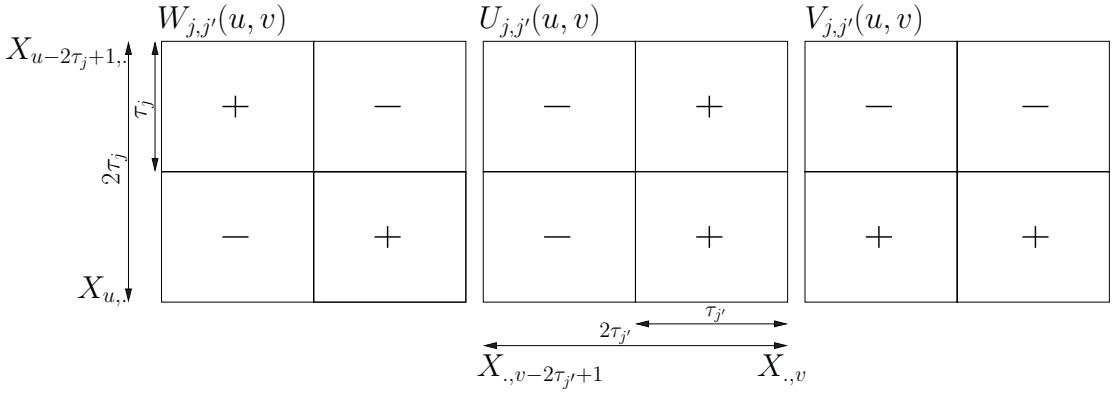


Figure 2: Illustration of two-dimensional wavelet coefficient operations on $X_{u,v}$ using the Haar wavelet at levels $j, j'$.

the input for a realization of $\{X_{u,v}\}$, resulting in coefficients $W_{j,j'}(u,v)$, $U_{j,j'}(u,v)$ and $V_{j,j'}(u,v)$ for levels $j, j'$ and $u > L_j, v > L_{j'}$. The coefficients are calculated on a block with upper left corner $X_{u-2\tau_j+1,v-2\tau_{j'}+1}$ and lower right corner $X_{u,v}$. This block is arranged in four non-overlapping sub-blocks of size $\tau_j \times \tau_{j'}$, each of which is averaged. The wavelet coefficients $W_{j,j'}$, $U_{j,j'}$ and $V_{j,j'}$ at location $(u,v)$ are then obtained as means of the corresponding signed sub-blocks shown in Fig. 2.

Paper I presents in detail how to calculate the coefficients in Eq. (1) – (4) for all possible combinations of levels $j, j'$ based on an efficient one-dimensional pyramid algorithm (see Percival and Walden, 2000, p. 178 for pseudo-code). The case of $j = j'$ is referred to as *diagonal* coefficients as the averaging and/or differencing operations are applied on the same scales horizontally and vertically. Note that this term was previously used by others (see, e.g., Lark and Webster, 2004) to describe the wavelet-wavelet coefficients from Eq. (1).

Let $\{C_{j,j'}(u,v)\}$ denote either coefficient process $\{W_{j,j'}(u,v)\}$, $\{U_{j,j'}(u,v)\}$, $\{V_{j,j'}(u,v)\}$ or $\{Z_{j,j'}(u,v)\}$ for levels $j, j'$. Then the wavelet variance is defined as

$$\nu^2_{C,j,j'} = \mathrm{var}\left\{C_{j,j'}(u,v)\right\}.$$

As shown in Mondal and Percival (2012b), for realizations of stationary or intrinsically stationary fields of dimension $(N,M)$, an unbiased estimator for the wavelet variance $\nu^2_{C,j,j'}$ is

$$\hat{\nu}^2_{C,j,j'} = \frac{1}{N_j M_{j'}} \sum_{u=L_j-1}^{N-1} \sum_{v=L_{j'}-1}^{M-1} C^2_{j,j'}(u,v), \tag{5}$$

where $N_j = N - L_j + 1$ and $M_{j'} = M - L_{j'} + 1$. There also exist other estimators for the wavelet variance, e.g., ones that are more robust towards contamination (Percival and Mondal, 2012; Mondal and Percival, 2012a). In Paper I both the unbiased estimator from Eq. (5) as well as a more robust estimator based on the median instead of the mean of the wavelet coefficients are presented along with the confidence intervals for the true unknown wavelet variances. They are applied to a spatiotemporal set of satellite images of sea ice, linking changes in statistical properties of the images with changes in physical properties of the ice.

## 1.2 SPATIOTEMPORAL INFECTIOUS DISEASE DATA

Together with several project partners, the Norwegian Centre for Integrated Care and Telemedicine (NST) hosts a project called Snow project (Bellika et al., 2007), named after the British physician and epidemiologist John Snow (1813-1858), with focus on medical data processing of distributed electronic health records. The Snow system is implemented in the Norwegian Health Network, which allows secure information exchange between healthcare professionals,

such as general practitioners, hospitals and laboratories. It consists of several services, including a real-time disease surveillance based on laboratory and syndromic disease data. Via the Snow client, available online at `snow.cs.uit.no`, also the general public is able to access epidemiological data in real-time.

In Paper III spatiotemporal infectious disease data are modeled for the North Norwegian counties Troms and Finnmark based on the microbiology laboratory data from UNN and thus contributing to the Snow project with information on how communicable diseases spread in this region, which in this thesis will be denoted as *North Norway* (contrary to the common usage of this term that, in addition, includes the county of Nordland). The region consists of $i = 1,...,44$ municipalities and is characterized by a sparse population. Cressie (1993) suggests that a lattice $D$ can be formed by an identifying feature unique for each municipality like their geographical center given by longitude $x_i$ and latitude $y_i$, i.e., $D = \{(x_i, y_i) : i = 1,...,44\}$. Another possibility is based on the adjacency structure between the municipalities, i.e., $D = \{(i, n_i) : i = 1,...,44\}$ with $n_i = \{j : j \sim i\}$ being the number of neighbors of municipality $i$, where neighborhood is defined as municipalities $i$ and $j$ sharing a common border.

North Norway is rather isolated at the top of continental Europe surrounded by the Norwegian sea and Barents sea towards the West and North, neighboring the Norwegian county Nordland as well as Sweden and Finland in the South, and having a short border with Russia in the East. There are only a few streets from Finland, one from Russia and none from Sweden directly accessing the considered region. Air traffic is a way of transportation, both within the region and from outside. Most air passengers from outside this region arrive to Tromsø, with its around 70000 inhabitants being by far the largest municipality in North Norway.

The microbiology laboratory data set of UNN covers person-to-person transmitted respiratory and gastrointestinal infectious diseases and contains information about

- Time (registration date in the laboratory, analysis date, date when the result was sent back to the test requester),
- Patient (gender, year of birth, postal and municipality code, hashed ID),
- Doctor's office requesting the analysis (postal and municipality code, hashed ID),
- Analysis (type, name, material, result).

Besides the test result (which can be either positive or negative) it is made use of registration date (the earliest possible date contained in this data set), patient year of birth (to derive the age as year of registration date minus the year of birth) and the municipality code of the test requesting doctor's office (as the patient's official registered municipality code might differ from the actual place of living). Furthermore, the hashed patient ID is needed to ensure a 90 day rule, i.e., further positive test results belonging to the same patient within 90 days are discarded.

Due to its high number of cases, influenza A is investigated in Paper III. The data set contains both the infectious agents for the general seasonal influenza A H3N2 and influenza A H1N1, commonly known as "swine flu". When the latter agent arose to an outbreak in 2009, initially it was registered in the laboratory database with the codes for general influenza A, such that the available influenza A data of the two agents H3N2 and H1N1 has to be considered as one entity in this setting. The data are aggregated to counts $y_{i,t}$ per municipality $i = 1,...,44$ and week $t = 1,...,234$ from 1 January 2008 to 25 June 2012.

Skrøvseth et al. (2012) used the microbiology data set from UNN for influenza A and pertussis cases to retrospectively detect outbreaks as changes in the disease incidence, with a causal formulation of the SiZer (Significant Zero Crossings of derivatives) scale-space methodology from Chaudhuri and Marron (1999). In Paper III scale is referred to in terms of geographic scale. Like in Brockmann et al. (2006), the number of humans traveling a distance $x$ is modeled as a power law, where the number of people decreases with increasing $x$. Movement network data are part of the model for spatiotemporal disease spread presented in Paper III. Here the influence of different power law approximations is investigated, both by regression fit based on actual traffic data and by the order of adjacency $o_{i,j}^{-d}$. The latter is determined by the adjacency structure between the municipalities $i$ and $j$ and power law coefficient $d \geq 0$.

# 2

# RESULTS AND DISCUSSION

## 2.1 PAPER I - WAVELET VARIANCE ESTIMATION

This paper, Geilhufe et al. (2013), presents an efficient calculation of two-dimensional MODWT coefficients for all levels $j, j'$ by an extended version of the one-dimensional pyramid algorithm. This forms the computational basis for the work in Paper II. Wavelet variance estimates and confidence intervals are given both for the mean and median case. Its usefulness is demonstrated on a spatiotemporal set of sea ice SAR images from the Arctic Ocean north of Alaska taken between November 1997 and October 1998 (see Stern and Moritz, 2002, for more information about the data set). Here, changes in statistical properties of the ice images are connected with changes in physical properties of the ice over the course of one year.

### 2.1.1 *Anisotropy in sea ice images*

In Paper I three sea ice images were analyzed more thoroughly, see Section 5 of Paper I including Fig. 5 for a visualization of the sea ice images. Henceforth, these are denoted as image 5a, 5b and 5c. The investigation in Paper I indicates that images 5a and 5c show some isotropic behavior, whereas 5b is seen as anisotropic. With the help of the wavelet-based test presented in Paper II, these images are tested for isotropy using the Haar wavelet (as in Paper I) and diagonal scales for levels $j = 1, ..., 9$. See Table 1 for the resulting p-values of the test statistic based on the ratio of the estimated diagonal scaling-wavelet and wavelet-scaling variance for level $j$, denoted as $\frac{\hat{\nu}^2_{U,j,j}}{\hat{\nu}^2_{V,j,j}}$. While none of the images is isotropic on every scale, it appears that 5a shows the most isotropic structure out of the three considered sea ice images. Here, the test does not reject the null hypothesis on a 5% significance level for four of the nine tested diagonal scales. There is no evidence against the assumption of isotropy on single levels $j = \{3, 7, 8, 9\}$. On the other hand,

Table 1: P-values for the single level test statistic based on diagonal sw/ws variance ratios using the isotropy test presented in Paper II on the sea ice images from Figure 5 in Paper I.

| | $\frac{\hat{\nu}^2_{U,1,1}}{\hat{\nu}^2_{V,1,1}}$ | $\frac{\hat{\nu}^2_{U,2,2}}{\hat{\nu}^2_{V,2,2}}$ | $\frac{\hat{\nu}^2_{U,3,3}}{\hat{\nu}^2_{V,3,3}}$ | $\frac{\hat{\nu}^2_{U,4,4}}{\hat{\nu}^2_{V,4,4}}$ | $\frac{\hat{\nu}^2_{U,5,5}}{\hat{\nu}^2_{V,5,5}}$ | $\frac{\hat{\nu}^2_{U,6,6}}{\hat{\nu}^2_{V,6,6}}$ | $\frac{\hat{\nu}^2_{U,7,7}}{\hat{\nu}^2_{V,7,7}}$ | $\frac{\hat{\nu}^2_{U,8,8}}{\hat{\nu}^2_{V,8,8}}$ | $\frac{\hat{\nu}^2_{U,9,9}}{\hat{\nu}^2_{V,9,9}}$ |
|---|---|---|---|---|---|---|---|---|---|
| 5a | < 0.0001 | < 0.0001 | 0.16 | < 0.0001 | 0.0001 | 0.015 | 0.40 | 0.85 | 0.18 |
| 5b | < 0.0001 | < 0.0001 | < 0.0001 | < 0.0001 | < 0.0001 | < 0.0001 | < 0.0001 | < 0.0001 | 0.03 |
| 5c | < 0.0001 | < 0.0001 | < 0.0001 | < 0.0001 | < 0.0001 | < 0.0001 | 0.011 | 0.03 | 0.018 |

images 5b and 5c are significantly anisotropic on all considered scales, though the significance is less for 5c on the highest levels $j = \{7, 8, 9\}$, i.e., there might be some but not enough isotropic structure on these scales $\tau_j$.

### 2.1.2 *Future work*

The methodology is not bound to monitoring of sea ice. Since Paper I comes with a `MATLAB` implementation for efficient two-dimensional MODWT coefficient calculation and wavelet variance estimation, it is open for everybody to use and might prove useful to several other applications, for instance in medical imaging. One possibility is the analysis of texture in pigmented skin lesion images, e.g., for monitoring benign lesions (Geilhufe et al., 2010) or for automatic detection of melanoma (Skrøvseth et al., 2010). Here, wavelet variance estimates at certain scales could be included as a feature for detecting changes.

## 2.2 PAPER II - WAVELET-BASED TEST FOR ISOTROPY

In this manuscript a test for isotropy on second-order stationary and intrinsically stationary random fields based on MODWT wavelet coefficients is presented. The test uses the property that under isotropy scaling-wavelet variances for levels $j, j'$ and wavelet-scaling variances for levels $j', j$ are the same, similarly wavelet-wavelet variances for $j, j'$ versus those for $j', j$, i.e.,

$$\nu^2_{U,j,j'} = \nu^2_{V,j',j} \quad \Leftrightarrow \quad \log\left(\frac{\nu^2_{U,j,j'}}{\nu^2_{V,j',j}}\right) = 0,$$
$$\nu^2_{W,j,j'} = \nu^2_{W,j',j} \quad \Leftrightarrow \quad \log\left(\frac{\nu^2_{W,j,j'}}{\nu^2_{W,j',j}}\right) = 0.$$

First, a single level test for the log-ratios is derived, followed by the more general simultaneous test over multiple ratios. The test statistic is $\chi^2$-distributed with $r$ degrees of freedom, $r$ being the number of ratios included. In order to perform the test, the basic wavelet filter, the maximum horizontal and vertical level $J$ and the log-ratios of interest have to be chosen. The asymptotics take effect already for small image sizes. In a simulation study on exponential, spherical and fractional Brownian fields, including comparison with existing methods (Guan et al., 2004; Lu and Zimmerman, 2005; Richard and Bierme, 2010), the presented test performs well concerning both the general applicability and its rejection rates. These are close to the nominal level for isotropic fields, and for anisotropic fields comparable to or exceeding the rejection rates of the other considered methods. Its practical usefulness is demonstrated on examples of mass density plots of paper handsheets.

### 2.2.1 *Other anisotropy types*

In the simulation studies of Paper II the test was applied only to fields exhibiting geometric anisotropy. This kind of anisotropy model is often used in spatial literature and is caused by axis stretching, shrinking and rotation, i.e., there exists a positive definite matrix $\boldsymbol{B}$ which linearly transforms an isotropic semivariogram $\gamma_0$ to an anisotropic semivariogram $\gamma(\boldsymbol{\kappa}) = \gamma_0\left(\sqrt{\boldsymbol{\kappa}^T\boldsymbol{B}\boldsymbol{\kappa}}\right)$ for all lags $\boldsymbol{\kappa} = (\kappa_1, \kappa_2) \in \mathbb{Z}^2$. Even though geometric anisotropy is the only spatial anisotropy type directly defined in, e.g., Cressie (1993), there also exist other types referred to as *zonal anisotropy* (Journel and Huijbregts, 1978; Chilès and Delfiner, 2012). A finer categorization was introduced by Zimmerman (1993):

- Sill anisotropy. It is caused by distinct sills (limiting value of a semivariogram) in different directions, i.e., $\lim_{\alpha\to\infty}\gamma(\alpha\frac{\boldsymbol{\kappa}}{||\boldsymbol{\kappa}||})$ varies for different $\frac{\boldsymbol{\kappa}}{||\boldsymbol{\kappa}||}, \boldsymbol{\kappa} \in \mathbb{Z}^2$, e.g., due to trends in the data or measurement errors.

- Range anisotropy. It is the case when the sill is equal in all directions, but attained at different distance for varying directions. There are two subgroups
  - Geometric (range) anisotropy.
  - Non-geometric range anisotropy. All range anisotropies that cannot be corrected by a linear transformation are categorized by this subgroup.

- Nugget anisotropy. The semivariogram's discontinuity at the origin (the so-called nugget effect) varies with direction, i.e., $\lim_{\alpha\to 0}\gamma(\alpha\frac{\boldsymbol{\kappa}}{||\boldsymbol{\kappa}||})$ varies for different $\frac{\boldsymbol{\kappa}}{||\boldsymbol{\kappa}||}, \boldsymbol{\kappa} \in \mathbb{Z}^2$. This can be caused by correlated measurement errors.

In the following a simulation study is created to see how the isotropy test from Paper II performs on anisotropic random fields that follow a sill and nugget anisotropy. Let the random field $Z_{u,v}$ be defined as $Z_{u,v} = X_{u,v} + Y_v$ for independent, stationary, zero mean processes $X_{u,v}$ and $Y_v$. Then the semivariogram of $Z_{u,v}$ is

$$\begin{aligned}
\gamma_{Z,\kappa_1,\kappa_2} &= \tfrac{1}{2}\mathrm{var}\{Z_{u,v} - Z_{u+\kappa_1,v+\kappa_2}\} \\
&= \tfrac{1}{2}E\{(X(u,v) - X(u+\kappa_1,v+\kappa_2))^2\} + \tfrac{1}{2}E\{(Y(v) - Y(v+\kappa_2))^2\} \\
&\quad + E\{(X(u,v) - X(u+\kappa_1,v+\kappa_2))(Y(v) - Y(v+\kappa_2))\} \\
&= \begin{cases} \gamma_{X,\kappa_1,\kappa_2} + \gamma_{Y,\kappa_2} & , \ \kappa_2 \neq 0 \\ \gamma_{X,\kappa_1,0} & , \ \kappa_2 = 0, \end{cases}
\end{aligned}$$

i.e., depending on $X_{u,v}$ and $Y_v$, the semivariogram for $Z_{u,v}$ may attain a different sill for $(\kappa_1, 0)$, the direction parallel to the first axis, than for all other directions, which corresponds to sill anisotropy.

Now let $X_{u,v}$ be a spherical field, and $Y_v$ either an exponential random process $Y_v^{(\exp)}$ or a Gaussian white noise process $Y_v^{\varepsilon}$, i.e.,

$$\gamma_{X,\kappa_1,\kappa_2} = \begin{cases} \lambda\left(\frac{3}{2m}||\boldsymbol{\kappa}|| - \frac{1}{2m^3}||\boldsymbol{\kappa}||^3\right) & \text{if } 0 \le ||\boldsymbol{\kappa}|| \le m \\ \lambda & \text{otherwise,} \end{cases} \tag{6}$$

$$\gamma_{Y^{(\exp)},\kappa_2} = \lambda\left(1 - \phi^{|\kappa_2|}\right), \tag{7}$$

$$\gamma_{Y^{\varepsilon},\kappa_2} = \begin{cases} \sigma_Y^2 & \text{if } |\kappa_2| > 0 \\ 0 & \text{otherwise,} \end{cases} \tag{8}$$

where $\lambda$ and $\sigma_Y^2$ are scale parameters and $m$ and $\phi$ smoothness parameters, with $0 < \phi < 1$ and $m > 0$. It follows from the reasoning above that $Z_{u,v}$ has a sill anisotropy for these processes. For the case of $Y_v^{\varepsilon}$ there is also nugget anisotropy in $Z_{u,v}$ as the nugget effect differs with direction,

$$\lim_{\alpha\to 0}\gamma_{Z,\alpha\kappa_1,\alpha\kappa_2} = \lim_{\alpha\to 0}\gamma_{X,\alpha\kappa_1,\alpha\kappa_2} + \lim_{\alpha\to 0}\gamma_{Y,\alpha\kappa_2} = \begin{cases} \sigma_Y^2 & \text{if } |\kappa_2| > 0 \\ 0 & \text{otherwise.} \end{cases}$$

For the simulation study, various parametrized fields $Z_{u,v}$ are generated, each with 1000 samples on $N \times N$ grids for $N = \{20, 40, 128\}$. The spherical process $X_{u,v}$ from Eq. (6) is parametrized with $\lambda = 1$ and $m = \{2, 5, 8\}$, the exponential process $Y_v^{(\exp)}$ from Eq. (7) with $\lambda = 1$ and $\phi = \{0.125, 0.500, 0.875\}$, and the white noise process $Y_v^{\varepsilon}$ from Eq. (8) with $\sigma_Y^2 = \{0.10, 0.25, 0.50, 0.75, 1.00\}$. Example realizations for $Z_{u,v} = X_{u,v} + Y_v$ are illustrated in Fig. 3 for a spherical field with $m = 5$ and above mentioned parametrizations for the process $Y_v$.

Like in the simulation studies performed in Paper II, the test is based on the D(4) wavelet and single level ratio $\hat{\nu}_{U,1,1}^2 / \hat{\nu}_{V,1,1}^2$. The results are displayed in Table 2. A high rejection rate of up to 100 % indicates a high power of the wavelet-based test in detecting anisotropy. Generally it can be concluded that increasing grid size and smoothness in $X_{u,v}$ yields better results. For $N = 128$ all fields were correctly rejected and for $N = 40$ with $m = 5$ and $m = 8$ between $97 - 100\%$. The lowest power of the test is achieved for anisotropy on the smallest grid in the construct of weakly correlated spherical fields with $m = 2$ added with a strongly correlated one-dimensional exponential process with $\phi = 0.875$ or added white noise along one dimension with low variance $\sigma_Y^2 = 0.10$. A grid of size $N = 20$ appears to be too small to capture the anisotropy here. However, the improvement with increasing $N$ confirms that the method works well if sufficient data are available.

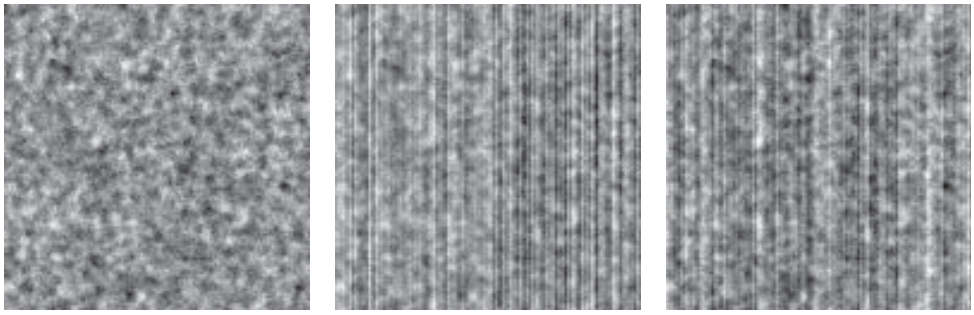

(a) isotropic (b) $\phi = 0.125$ (c) $\phi = 0.500$

(d) $\phi = 0.875$ (e) $\sigma_Y^2 = 0.1$ (f) $\sigma_Y^2 = 0.25$

(g) $\sigma_Y^2 = 0.50$ (h) $\sigma_Y^2 = 0.75$ (i) $\sigma_Y^2 = 1.00$

Figure 3: Example realizations of random fields $Z_{u,v} = X_{u,v} + Y_v$ with sill anisotropy, constructed from isotropic spherical field $X_{u,v}$ with $m = 5$ (a) and exponential process $Y_v^{\text{exp}}$ with $\phi = \{0.125, 0.500, 0.875\}$ (b,c,d) or white noise process $Y_v^{\varepsilon}$ with $\sigma_Y^2 = \{0.10, 0.25, 0.50, 0.75, 1.00\}$ (e,f,g,h,i). For illustration purposes the underlying spherical field $X_{u,v}$ is generated with equal random seed.

Table 2: Rejection rates in % for different sill anisotropic spherical fields of size $N$, each based on 1000 simulations.

| | | | $\mathbf{Y}_{\mathbf{v}}^{(\exp)}$, $\phi$ | | | $\mathbf{Y}_{\mathbf{v}}^{(\varepsilon)}$, $\sigma_{\mathbf{Y}}^{\mathbf{2}}$ | | | | |
|---|---|---|---|---|---|---|---|---|---|---|
| | **N** | **m** | **0.125** | **0.500** | **0.875** | **0.10** | **0.25** | **0.50** | **0.75** | **1.00** |
| $\mathbf{X}_{\mathbf{u},\mathbf{v}}^{(\text{spherical})}$ | **20** | **2** | 91.8 | 73.8 | 12.8 | 11.7 | 36.0 | 70.5 | 85.0 | 94.0 |
| | | **5** | 99.8 | 98.9 | 48.7 | 46.1 | 88.6 | 98.3 | 99.4 | 99.7 |
| | | **8** | 100 | 99.8 | 77.8 | 72.7 | 97.5 | 99.5 | 100 | 100 |
| | **40** | **2** | 100 | 99.9 | 52.9 | 49.4 | 94.2 | 100 | 100 | 100 |
| | | **5** | 100 | 100 | 98.0 | 97.1 | 100 | 100 | 100 | 100 |
| | | **8** | 100 | 100 | 100 | 99.7 | 100 | 100 | 100 | 100 |
| | **128** | **2** | 100 | 100 | 100 | 100 | 100 | 100 | 100 | 100 |
| | | **5** | 100 | 100 | 100 | 100 | 100 | 100 | 100 | 100 |
| | | **8** | 100 | 100 | 100 | 100 | 100 | 100 | 100 | 100 |

### 2.2.2 *Future work*

Even though the wavelet-based test is able to detect anisotropy on different scales, the test in Paper II was used globally such that every test statistic indicates presence of isotropy or anisotropy only for the entire image. As wavelet variances were already used successfully for texture classification and segmentation by Unser (1995), a natural extension would be to use the presented test locally on smaller regions of an image. The idea then is that different textures yield different degrees of anisotropy, which may result in a new useful measure for texture analysis.

## 2.3 PAPER III - MODELING INFECTIOUS DISEASE SPREAD

Based on microbiology laboratory data from the University Hospital of North Norway, in Paper III the disease spread of influenza A in the 44 Norwegian municipalities of the Northernmost counties Troms and Finnmark is described with observation-driven (OD) models. The model framework of interest is the one introduced by Held et al. (2005) and extended by Paul et al. (2008); Paul and Held (2011); Held and Paul (2012). It decomposes the disease incidence into an endemic and epidemic component, the latter consisting of an autoregressive and a spatiotemporal component. Each component allows for fixed, random and seasonal effects, where in this study a baseline model for influenza from Held and Paul (2012) is followed and extended with covariates accounting for population in each municipality, immigration from outside the study region or the proportion of positive laboratory tests as a way to capture reporting bias.

The spatiotemporal component of the OD model relates the disease incidence over different regions, specified for two municipalities $i$ and $j$ by weights $w_{i,j}$. The focus of Paper III is to investigate different weights that approximate human travel patterns with a power law approach, both by regression of the travel data (based on air, road and sea traffic) and by the adjacency structure of the considered municipalities.

The power law approach is motivated by Brockmann et al. (2006), who tracked dollar bills in the United States and approximated human travel by a power law. Paper III suggests that the presented approach is also a useful way to capture spatiotemporal disease spread. Based on proper scoring rules (Czado et al., 2009) for model comparisons using one-step-ahead predictions for the considered spatiotemporal disease data, power law approximated weights yield better or comparable results to actual traffic counts.

### 2.3.1 *Parameter-driven model*

In Paper III the disease incidence is modeled with an observation-driven approach. Another possibility is to use a parameter-driven (PD) model. Here, the disease incidence is driven by an unobserved autocorrelation (Zeger and Qaqish, 1988), where an hierarchical Bayesian approach (Banerjee et al., 2003) for inference appears useful (Schrödle et al., 2012). Computationally it is not feasible to adapt the baseline OD model into a PD model. A dynamic model as in Schrödle et al. (2012) is the closest adaption of the OD approach, but with the restriction of a fixed autoregressive parameter.

The general model setup is as follows. For weeks $t = 1,...,234$ and municipalities $i = 1,...,44$ the number $y_{i,t}$ of positive influenza A laboratory counts is modeled as

$$y_{i,t} \sim \text{Poisson}(E_{i,t} \exp(\eta_{i,t})),$$

with an offset $E_{i,t}$, like in the OD model in Paper III, accounting for the population sizes in each municipality $i$ in the year of week $t$ and

$$\eta_{i,t} = \alpha + \zeta_{i,t} + \nu_i + c_t \tag{9}$$

$$\zeta_{i,t} = \lambda \zeta_{i,t-1} + \varepsilon_{i,t}, \tag{10}$$

where $\eta_{i,t}$ is the sum of an intercept $\alpha$, vector autoregressive process $\zeta_i = (\zeta_{i,1},...\zeta_{i,t})^T$, spatial component $\nu_i$ and seasonal component $c_t = \gamma \sin(2\pi t/52) + \delta \cos(2\pi t/52)$. Covariates $z_{i,t}$ can be added in Eq. (9), but they are not considered here. The autoregressive process in Eq. (10) is of order 1, where

$$\zeta_{i,1} \sim \mathcal{N}\left(0, \frac{1}{\tau_\varepsilon(1-\lambda^2)}\right),$$

with independent and identically distributed (iid) Gaussian errors $\varepsilon_{i,t} \sim \mathcal{N}(0, \tau_\varepsilon^{-1})$ and unknown precision $\tau_\varepsilon$. The spatial component $\nu_i$ is formulated as an intrinsic Gaussian Markov Random Field (Rue and Held, 2005) with weighted averages as in (Kneib, 2006, Eq. (4.26)),

$$(\nu_i|\nu_{-i}, \tau_\nu) \sim \mathcal{N}\left(\sum_{j:j\sim i} \frac{w_{i,j}}{n_i}\nu_j, \frac{1}{\tau_\nu n_i}\right),\ n_i = \sum_{j:j\sim i} w_{i,j},\ i \neq j,$$

with weights $w_{i,j}$ and unknown precision $\tau_\nu$. Note that the weights are now used to describe the spatial dependence between municipalities. This is in contrast to the OD model presented in Paper III, where weights describe travel patterns in the spatiotemporal component. Incorporation of weights in a multivariate latent Gaussian process of a parameter-driven model, as proposed in Schrödle et al. (2012) for a much shorter time-series and a single one-step-ahead prediction, turned out to be computationally infeasible.

To perform approximate Bayesian inference in this latent Gaussian model, integrated nested Laplace approximations (INLA) developed by Rue et al. (2009) are used, which is implemented in the `R` package `INLA`, available at `http://www.r-inla.org/`. The weights are incorporated with some adaptions to the different symmetric weight matrices $\mathbf{W}_1$, $\mathbf{W}_2$ and $\mathbf{W}_{3,d}$ presented in Paper III. Diagonal entries are the row sums of the former weight matrix and all off-diagonal entries are negative such that rows and columns sum to zero.

As in Paper III, one-step-ahead predictions for the last 78 weeks of the influenza A data are evaluated for the differently weighted models with proper scoring rules for count data (Czado et al., 2009) in form of the logarithmic score (logS), ranked probability score (RPS) and squared error score (SES). A lower score corresponds to a better model. The results are displayed in Table 3. Weights of type $\mathbf{W}_3$ are only displayed for power law coefficient $d = 1$ as the result was nearly identical for other coefficients $d = \{0, 1/2, 2, \infty\}$. The scores for $\mathbf{W}_1$, $\mathbf{W}_2$ and $\mathbf{W}_{3,d=1}$ are very similar with no substantial difference, but there is a weak evidence for a lower SES with the power law regression weight $\mathbf{W}_2$. In general, it can be concluded that in this setting weights do not have such a strong influence as for the OD models.

Table 3: Scores for the PD model with spatial weights $\mathbf{W}_1$, $\mathbf{W}_2$ and $\mathbf{W}_{3,d=1}$ based on one-step-ahead predictions for influenza A counts. Monte Carlo p-values based on 9999 permutations from a separate comparison using the PD model with $\mathbf{W}_1$ are given in parentheses.

| **Weight** | **logS** | (p-value) | **RPS** | (p-value) | **SES** | (p-value) |
|---|---|---|---|---|---|---|
| $\mathbf{W}_1$ | 0.2188 | | 0.1058 | | 0.4652 | |
| $\mathbf{W}_2$ | 0.2187 | (0.41) | 0.1057 | (0.22) | 0.4591 | (0.11) |
| $\mathbf{W}_{3,d=1}$ | 0.2188 | (0.41) | 0.1058 | (0.58) | 0.4648 | (0.53) |

Comparing the scores of the here presented PD model with the baseline OD model from Paper III, the observation-driven approach generally yields better results based on logS and RPS. Using SES, the PD model appears superior. Fig. 4 shows the influenza A disease counts for the last 78 weeks of the time-series together with the weekly mean one-step-ahead predictions for both the baseline OD and PD model using weights $\mathbf{W}_1$, over all municipalities and separately for the three most populous ones, i.e., Tromsø, Harstad and Alta. As indicated by SES, the mean values of the PD model are somewhat better predictors than those of the OD model. However, SES only incorporates the mean and not the dispersion of the predictive distribution, while the other two scores (logS and RPS) incorporate both sharpness and calibration (Gneiting and Raftery, 2007).

### 2.3.2 *Future work*

It would be interesting to perform a similar type of analysis for some other region, preferably one that is not so sparsely populated. The potential lack of actual traffic data could be overcome by adjacency-based power law formulations. A possible extension to the presented approach in Paper III is to include the power law coefficient estimation in the regression of the OD model instead of fixing it to a certain $d$. If actual traffic data are available, then the power law fit of this data could be part of the OD model. In this way one would account for uncertainty in the estimation of the weights.

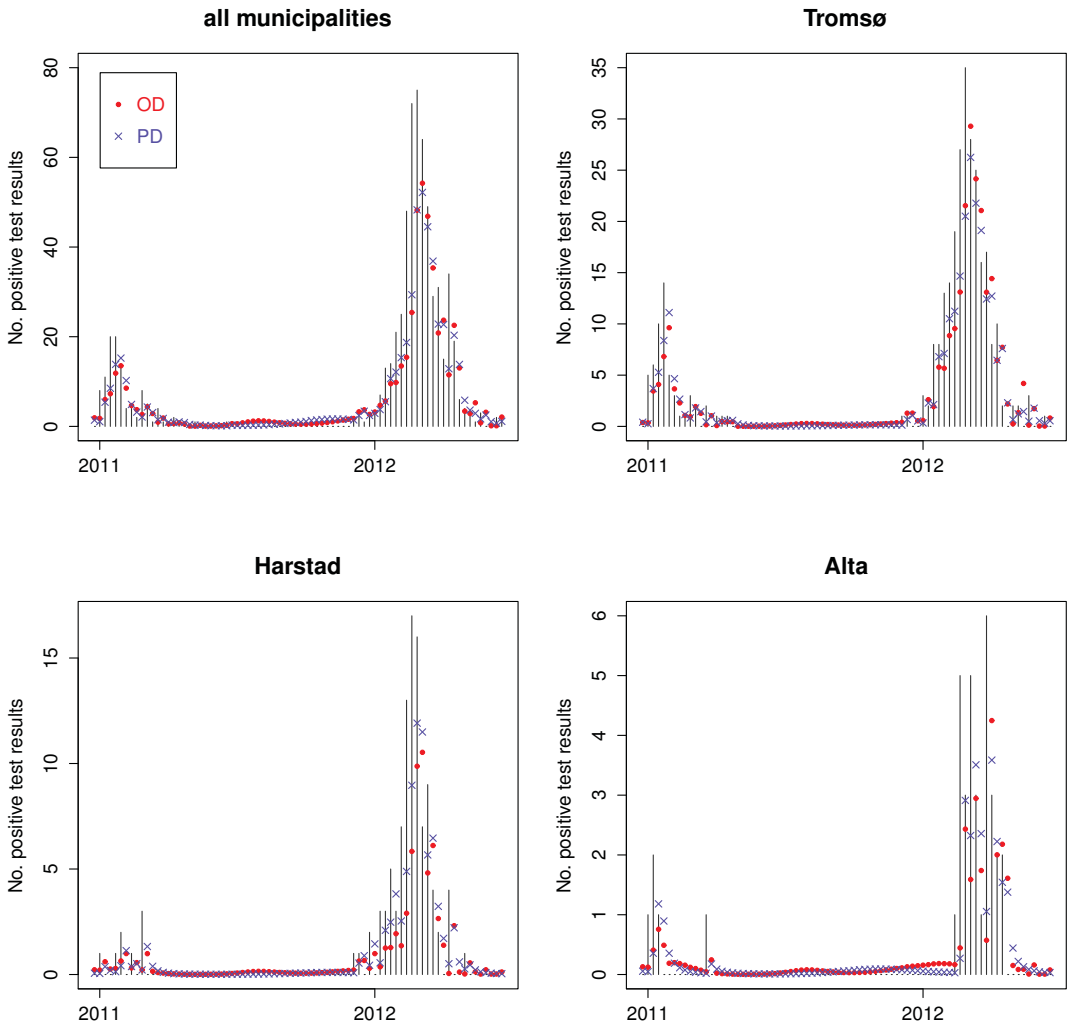


Figure 4: Mean of the one-step ahead influenza A disease count predictions summed over all municipalities (top left), for Tromsø (top right), Harstad (bottom left) and Alta (bottom right) using the baseline OD (red dots) and PD model (blue crosses) with weights $\mathbf{W}_1$. The actual disease counts are shown as black bars.

# BIBLIOGRAPHY


Banerjee, S., Gelfand, A. E., Carlin, B. P., 2003. Hierarchical modeling and analysis for spatial data. Chapman and Hall/CRC, Boca Raton, FL, USA.

Bellika, J. G., Hasvold, T., Hartvigsen, G., 2007. Propagation of program control: A tool for distributed disease surveillance. International Journal of Medical Informatics 76 (4), 313–329.

Brockmann, D., Hufnagel, L., Geisel, T., 2006. The scaling laws of human travel. Nature 439 (7075), 462–465.

Chaudhuri, P., Marron, J., 1999. Sizer for exploration of structures in curves. Journal of the American Statistical Association 94 (447), 807–823.

Chilès, J. P., Delfiner, P., 2012. Geostatistics: Modeling spatial uncertainty, 2nd Edition. John Wiley & Sons, Inc., Hoboken, NJ, USA.

Cressie, N., 1993. Statistics for spatial data, Revised Edition. John Wiley & Sons, Inc., New York, NY, USA.

Czado, C., Gneiting, T., Held, L., 2009. Predictive model assessment for count data. Biometrics 65 (4), 1254–1261.

Daubechies, I., 1992. Ten Lectures on Wavelets. Cbms-Nsf Regional Conference Series in Applied Mathematics. Society for Industrial and Applied Mathematics (SIAM), Philadelphia, PA, USA.

Gaetan, C., Guyon, X., 2010. Spatial Statistics and Modeling. Springer, New York, NY, USA.

Geilhufe, M., Percival, D. B., Stern, H. L., 2013. Two-dimensional wavelet variance estimation with application to sea ice SAR images. Computers & Geosciences 54, 351–360.

Geilhufe, M., Skrøvseth, S. O., Godtliebsen, F., 2010. Digital monitoring of changes in skin lesions. In: IADIS International Conference e-Health. Freiburg, Germany, pp. 229–233.

Gneiting, T., Raftery, A. E., 2007. Strictly proper scoring rules, prediction, and estimation. Journal of the American Statistical Association 102 (477), 359–378.

Gonzalez, R. C., Woods, R. E., 2008. Digital Image Processing, 3rd Edition. Pearson Education, Inc., Upper Saddle River, NJ, USA.

Guan, Y., Sherman, M., Calvin, J. A., 2004. A nonparametric test for spatial isotropy using subsampling. Journal of the American Statistical Association 99 (467), 810–821.

Held, L., Höhle, M., Hofmann, M., 2005. A statistical framework for the analysis of multivariate infectious disease surveillance counts. Statistical Modelling 5 (3), 187–199.

Held, L., Paul, M., 2012. Modeling seasonality in space-time infectious disease surveillance data. Biometrical Journal 54 (6), 824–843.

Journel, A. G., Huijbregts, C. J., 1978. Mining Geostatistics. Academic Press, London, UK.

Kneib, T., 2006. Mixed model based inference in structured additive regression. Ph.D. thesis, Ludwig Maximilians University Munich, Germany.

Lark, R. M., Webster, R., 2004. Analysing soil variation in two dimensions with the discrete wavelet transform. European Journal of Soil Science 55 (4), 777–797.

Lawson, A. B., 2006. Statistical methods in spatial epidemiology., 2nd Edition. John Wiley & Sons, Ltd, Chichester, UK.

Lu, N., Zimmerman, D. L., 2005. Testing for directional symmetry in spatial dependence using the periodogram. Journal of Statistical Planning and Inference 129, 369–385.

Mondal, D., Percival, D. B., 2012a. M-estimation of wavelet variance. Annals of the Institute of Statistical Mathematics 64 (1), 27–53.

Mondal, D., Percival, D. B., 2012b. Wavelet variance analysis for random fields on a regular lattice. IEEE Transactions on Image Processing 21 (2), 537–549.

Paul, M., Held, L., 2011. Predictive assessment of a non-linear random effects model for multivariate time series of infectious disease counts. Statistics in Medicine 30 (10), 1118–1136.

Paul, M., Held, L., Toschke, A. M., 2008. Multivariate modelling of infectious disease surveillance data. Statistics in Medicine 27 (29), 6250–6267.

Percival, D. B., Mondal, D., 2012. A wavelet variance primer. In: Subba Rao, T., Rao, C. (Eds.), Handbook of Statistics. Vol. 30: Time Series. Elsevier, Oxford, UK, Ch. 22, pp. 623–659.

Percival, D. B., Walden, A. T., 2000. Wavelet Methods for Time Series Analysis. Cambridge University Press, New York, NY, USA.

Richard, F., Bierme, H., 2010. Statistical tests of anisotropy for fractional Brownian textures. Application to full-field digital mammography. Journal of Mathematical Imaging and Vision 36 (3), 227–240.

Ripley, B. D., 1981. Spatial Statistics. John Wiley & Sons, Inc., Hoboken, NJ, USA.

Rue, H., Held, L., 2005. Gaussian Markov Random Fields: Theory and Applications. Chapman & Hall, London, UK.

Rue, H., Martino, S., Chopin, N., 2009. Approximate bayesian inference for latent gaussian models using integrated nested laplace approximations. Journal of the Royal Statistical Society, Series B 71 (2), 319–392.

Schrödle, B., Held, L., Rue, H., 2012. Assessing the impact of a movement network on the spatiotemporal spread of infectious diseases. Biometrics 68 (3), 736–744.

Skrøvseth, S. O., Bellika, J. G., Godtliebsen, F., 2012. Causality in scale space as an approach to change detection. PLoS ONE 7 (12), e52253, 1–14.

Skrøvseth, S. O., Schopf, T., Thon, K., Zortea, M., Geilhufe, M., Mollersen, K., Kirchesch, H., Godtliebsen, F., 2010. A computer aided diagnostic system for malignant melanomas. In: 3rd International Symposium on Applied Sciences in Biomedical and Communication Technologies. Rome, Italy, pp. 1–5.

Stern, H. L., Moritz, R. E., 2002. Sea ice kinematics and surface properties from RADARSAT synthetic aperture radar during the SHEBA drift. Journal of Geophysical Research 107 (C10), SHE 14, 1–10.

Unser, M., 1995. Texture classification and segmentation using wavelet frames. IEEE Transactions on Image Processing 4 (11), 1549–1560.

Zeger, S. L., Qaqish, B., 1988. Markov regression models for time series: A quasi-likelihood approach. Biometrics 44 (4), 1019–1031.

Zimmerman, D. L., 1993. Another look at anisotropy in geostatistics. Mathematical Geology 25 (4), 453–470.

# Part II

# PAPERS

**Paper I**

Two-dimensional wavelet variance estimation with application to sea ice SAR images

**Geilhufe, M., Percival, D. B. and Stern, H. L.**

*Computers & Geosciences*, 2013, Vol. 54, pp. 351-360

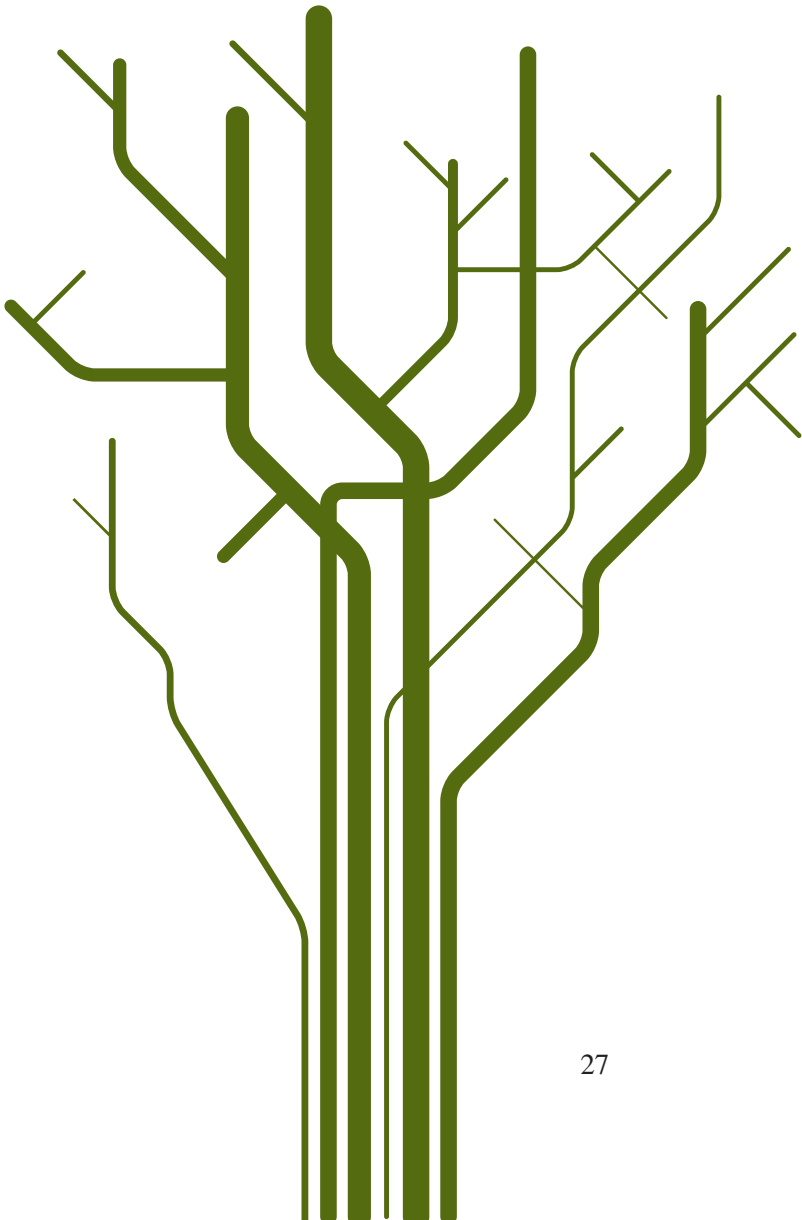

**Paper II**

A multiscale wavelet-based test for isotropy of random fields on a regular lattice

**Thon K., Geilhufe, M. and Percival, D. B.**

submitted to *IEEE Transactions on Image Processing*

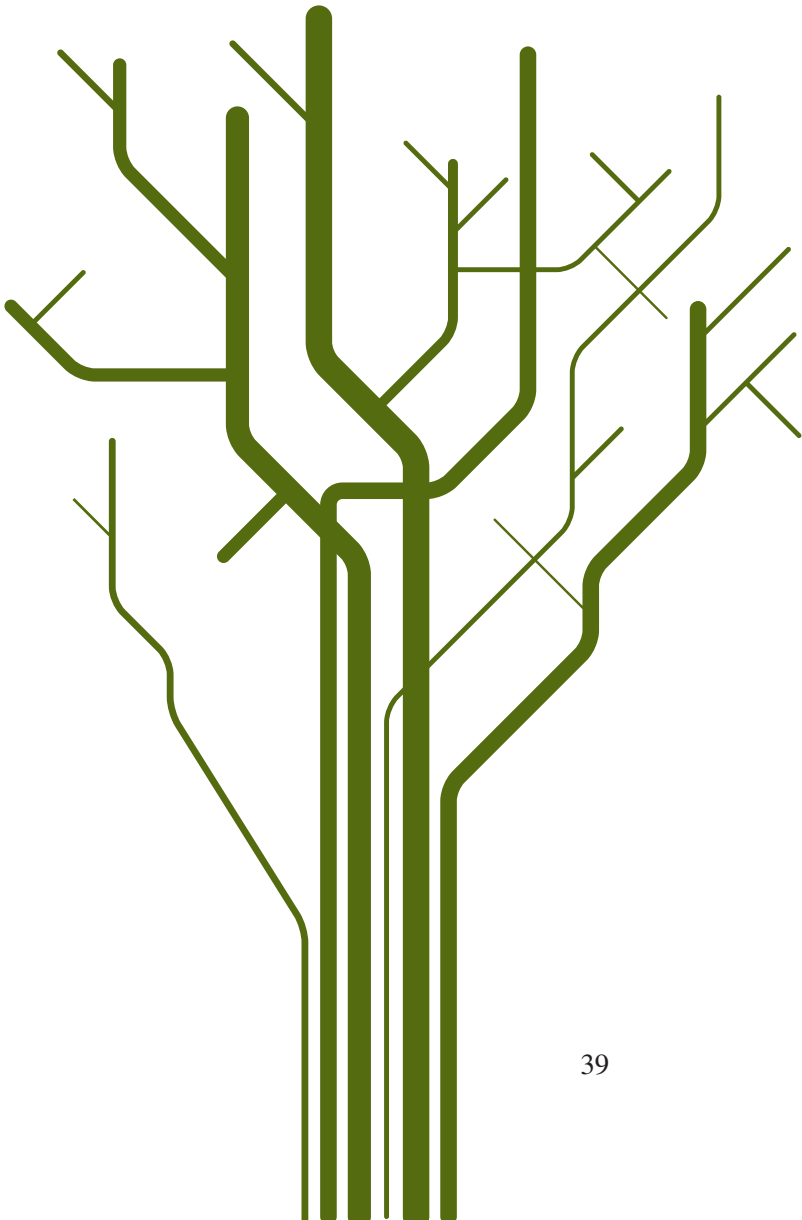

**Paper III**

Power law approximations of movement network data for modeling infectious disease spread

**Geilhufe, M., Held, L., Skrøvseth, S. O., Simonsen, G. S. and Godtliebsen, F.**

revised and re-submitted to *Biometrical Journal*